engineering proceedings

MDPI

Proceeding Paper

Hyperspectral Analysis of Apricot Quality Parameters Using Classical Machine Learning and Deep Neural Networks †

Martin Dejanov

Department of Automation and Electronics, University of Ruse, 7017 Ruse, Bulgaria; mdejanov@uni-ruse.bg

† Presented at the International Conference on Electronics, Engineering Physics and Earth Science (EEPES 2025), Alexandroupolis, Greece, 18–20 June 2025.

Abstract

This study focuses on predicting β-carotene content using hyperspectral images captured in the near-infrared (NIR) region during the drying process. Several machine learning models are compared, including Partial Least Squares Regression (PLSR), Stacked Autoencoders (SAEs) combined with Random Forest (RF), and Convolutional Neural Networks (CNNs) in three configurations: 1D-CNN, 2D-CNN, and 3D-CNN. The models are evaluated using R^2, Mean Absolute Error (MAE), and Root Mean Squared Error (RMSE). The PLSR model showed excellent results with R^2 = 0.97 for both training and testing, indicating minimal overfitting. The SAE-RF model also performed well, with R^2 values of 0.82 and 0.83 for training and testing, respectively, showing strong consistency. The CNN models displayed varying results: 1D-CNN achieved moderate performance, while 2D-CNN and 3D-CNN exhibited signs of overfitting, especially on testing data. Overall, the findings suggest that although CNNs are capable of capturing complex patterns, the PLSR and SAE-RF models deliver more reliable and robust predictions for β-carotene content in hyperspectral imaging.

Keywords: hyperspectral imaging; regression models; machine learning; deep learning; β-carotene content; apricot quality parameters

check for updates

Academic Editor: Grigor Mihaylov

Published: 25 August 2025

Citation: Dejanov, M. Hyperspectral Analysis of Apricot Quality Parameters Using Classical Machine Learning and Deep Neural Networks. *Eng. Proc.* **2025**, *104*, 24. https://doi.org/10.3390/engproc2025104024

Copyright: © 2025 by the author. Licensee MDPI, Basel, Switzerland. This article is an open access article distributed under the terms and conditions of the Creative Commons Attribution (CC BY) license (https://creativecommons.org/licenses/by/4.0/).

1. Introduction

In the modern food industry, ensuring high-quality products is a critical issue, as consumers expect food items that meet high standards while remaining affordable. To maintain these quality standards, producers must implement effective detection techniques and methodologies to guarantee product consistency and safety. One of the emerging technologies in this domain is hyperspectral imaging (HSI), which has attracted significant interest across multiple disciplines, including remote sensing, medical science, food quality assessment, and plant disease detection [1–4]. Due to its high spectral resolution and information-rich content, hyperspectral imaging has become an essential tool for various applications such as environmental monitoring, agricultural production, and mineral exploration. The ability to extract valuable spectral features from hyperspectral data has led to its growing adoption in food quality analysis. However, the complexity of hyperspectral datasets, which consist of hundreds of spectral bands, requires advanced computational approaches to extract meaningful information efficiently. Traditional methods such as Principal Component Analysis (PCA), Independent Component Analysis (ICA), and Linear Discriminant Analysis (LDA) have been used to process spectral information by reducing dimensionality and selecting the most representative spectral features. Despite

their usefulness, these methods struggle to capture the nonlinear relationships inherent in hyperspectral data, leading to limitations in classification and regression accuracy [4]. To overcome these challenges, machine learning algorithms, including PLS (Partial Least Square), Support Vector Machines (SVM), k-Nearest Neighbors (k-NN), and Naïve Bayes, have been applied to hyperspectral data analysis. However, these traditional machine learning techniques often require extensive feature engineering and are limited by their ability to generalize to complex, high-dimensional datasets. In recent years, deep learning techniques have gained traction in the field of hyperspectral imaging due to their ability to automatically learn hierarchical features and extract complex patterns from data [5]. Compared to traditional machine learning models, deep learning methods become more robust as the number of layers increases, allowing them to achieve superior classification performance. Convolutional Neural Networks (CNNs) have been widely adopted for hyperspectral image analysis, particularly in applications such as plant species classification for 30 plant species from live-crown images [6,7]. Nie et al. demonstrated that CNNs outperformed Partial Least Squares Discriminant Analysis (PLS-DA) and Support Vector Machines (SVM) in identifying hybrid vegetable varieties [8]. Similarly, Yu et al. proposed a novel deep learning framework combining CNNs and Stacked Sparse Autoencoders (SSAEs) to classify hybrid okra seeds. Their experiments, conducted on a dataset containing 18,931 samples from 18 okra varieties, revealed that CNN-based models achieved the highest accuracy (93.79%) compared to traditional machine learning approaches such as Extreme Learning Machine (ELM) and Backpropagation Neural Networks (BPNN) [9]. A key advancement in deep learning applications for hyperspectral imaging is the use of saliency maps, a visualization technique that highlights the most influential features for model predictions [10]. Originally designed for 2D image analysis, saliency maps have been extended to multi-dimensional data, providing valuable insights into spectral feature importance. Shen et al. utilized saliency maps for maturity degree identification, demonstrating their potential in enhancing the interpretability of deep learning models in hyperspectral analysis [11]. Beyond plant classification and food quality assessment, hyperspectral imaging has also been employed in disease detection. Zhu et al. used hyperspectral data to study short-term tobacco mosaic virus infections, achieving a classification accuracy of 95% using neural network models [12]. This study highlights the effectiveness of hyperspectral imaging in detecting subtle biochemical changes that are often imperceptible to the human eye. As hyperspectral imaging continues to evolve, its integration with deep learning methods offers promising opportunities for improving food quality assessment. While traditional machine learning approaches have laid the groundwork for hyperspectral data analysis, deep learning techniques provide superior feature extraction and classification capabilities. Given the growing body of research in this field, further advancements in neural network architectures and computational efficiency will likely enhance the applicability of hyperspectral imaging in the food industry and beyond.

2. Materials and Methods

The aim of the research is to evaluate the content of β-carotene in the process of drying using hyperspectral characteristics of the apricots obtained in the NIR spectral region (900–1700 nm). To achieve the goal, some predictive models were developed using linear and non-linear regression methods based on classical machine learning and artificial neural networks.

2.1. Sample Preparation and Reference Measurement

The apricot samples used in this study were obtained from local markets in Ruse, Bulgaria. The selected variety, New Jersey, was cut into halves and subjected to a con-

trolled drying process in an oven at a fixed temperature of 65 °C with an air circulation speed of 2 m/s. To assess β-carotene content throughout the drying process, reference measurements were conducted in a laboratory environment using the internally validated chromatographic quantification method LC-17/2017. Samples were collected at three distinct time points, yielding the following β-carotene concentrations:

- A total of 210 mg/kg DM at the first time point;
- A total of 93 mg/kg DM at the second time point;
- A total of 41 mg/kg DM at the third time point.

To evaluate apricot quality throughout the drying process, hyperspectral characteristics were recorded within the near-infrared (NIR) spectrum. The experiment involved acquiring 32, 24, and 40 hyperspectral images per sample, with images captured from both sides of each apricot, as previously described.

The hyperspectral imaging (HSI) system employed in this research consisted of the following components:

- Imaging spectrograph: Imspector V17E (Spectral Imaging Ltd., Oulu, Finland);
- Camera: CCD camera–Goldeye CL-008 SWIR Cool (Spectral Imaging Ltd., Oulu, Finland);
- Illumination: Four 50 W halogen lamps (Osram, Ruse, Bulgaria);
- Software: SpectralDAQ-NIR v.1 (Spectral Imaging Ltd., Oulu, Finland);
- Mechanical system: Electronically controlled displacement platform (Ezi-Servo, Ruse, Bulgaria)

The representation of the system is depicted in Figure 1.

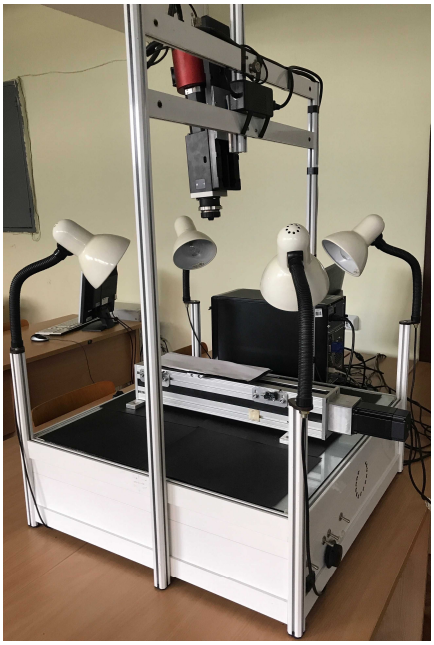


Figure 1. Hyperspectral imaging system.

To ensure the clarity and accuracy of the hyperspectral images obtained by the HSI system, key imaging parameters were carefully adjusted. These parameters included the exposure time, the distance between the lens and the apricot samples, and the conveyor speed. The apricot samples were placed on a white plate to eliminate background interference. The plate was positioned on a moving conveyor belt, enabling seamless hyperspectral image acquisition. During each line scan of the HSI system, a three-dimensional (3D) hypercube was generated, consisting of two-dimensional (2D) spatial information and one-dimensional (1D) spectral data, covering a succession of wavebands predefined by the HSI system.

2.2. Hyperspectral Image Data Acquisition and Preprocessing

In the study, hyperspectral images were acquired with a maximum spectral resolution of 256 wavelengths and a spatial resolution of 320 pixels per line. Images were taken on a batch, as it is shown in Figure 2. The RGB representation of hyperspectral images in the Near-Infrared (NIR) range, captured during the drying process, is presented there as three types of classes are shown. These hyperspectral images were classified into three distinct categories based on the measured β-carotene content. The data, derived from the drying process, are further discussed in [13].

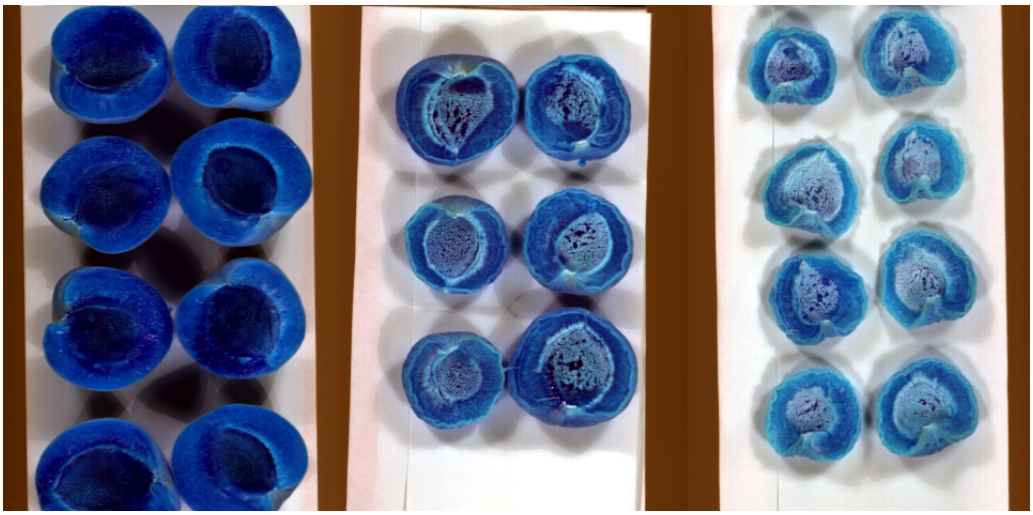
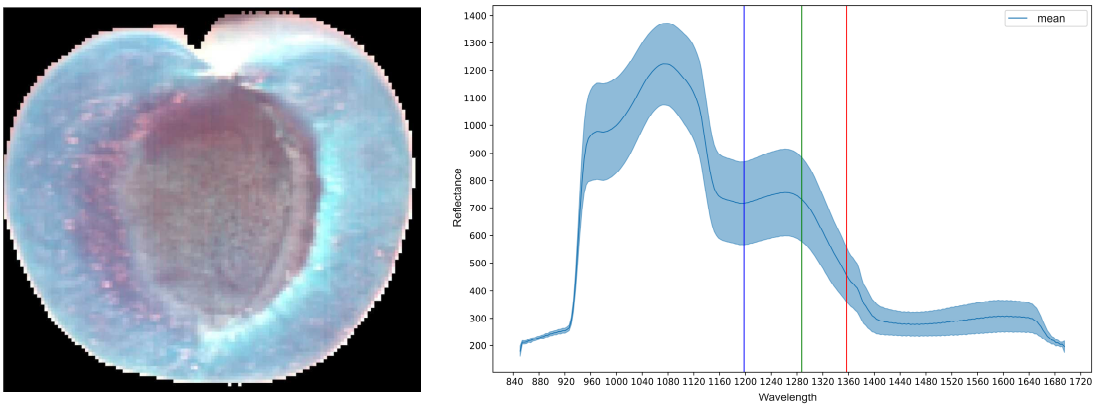


Figure 2. RGB representation of hyperspectral image for three types of classes.

After obtaining the hyperspectral images, they were preprocessed by taking them one by one and removing the background as it is shown in Figure 3a. It illustrates a representative sample element, showcasing the mean spectrum characteristic and the range of change in spectral reflectance across the entire surface of the image in Figure 3b.



(**a**) (**b**)

Figure 3. (**a**) RGB representation of a hyperspectral image of an apricot and (**b**) the mean spectrum characteristic and the range of change in spectral reflectance.

The images were then preprocessed. First, the reflectance values in the HSI dataset were scaled to have a mean of 0 and a standard deviation of 1, but only for the data used in the PLSR model. For the 1D-CNN and SAE-RF models, the mean spectrum was used instead. After that, the pixel vectors were used to train different types of models. For the training of the 2D-CNN and 3D-CNN models, all spectral characteristics were fed into the convolutional networks without any preprocessing.

2.3. Predictive Models

Regression analysis was used to evaluate how well predictive variables (X) explain variations in dependent variables (Y) with different neural networks and machine learning methods. Regression models estimate unknown values based on known data, and in this study, they were developed to predict β-carotene concentrations in apricots using hyperspectral imaging. Reference measurements on solutions with known concentrations were used for model calibration. These models offer a cost-effective alternative to direct chemical analysis, particularly in cases where direct measurement is challenging or expensive. In this study two types of models were used:

- standard machine learning models—PLSR and Stacked Autoencoders (SAEs) in combination with Random Forest (RF);
- convolutional neural networks: Convolutional Neural Networks (CNNs) in 1D, 2D, and 3D configurations.

Model performance was evaluated during training with R_t^2, MAE_t, and $RMSE_t$, and during testing with R_p^2, MAE_p, and $RMSE_p$, providing insights into predictive accuracy and model generalization.

2.4. Partial Least Square Regression (PLSR)

Partial Least Squares Regression (PLSR) is a statistical technique combining linear regression and dimensionality reduction, like PCA. It's especially useful for high-dimensional datasets with multicollinearity and limited samples, common in hyperspectral image evaluation. PLSR constructs latent variables that maximize covariance between predictors (e.g., spectral bands) and response variables (e.g., concentrations of β-carotene). PLSR emphasizes the relationship between predictors and response variables, making it suitable for regression tasks like this. PLSR is widely used in agriculture and food industries for nondestructive quality assessment, including evaluating ripeness, sugar content, and other biochemical properties through hyperspectral analysis [14–16]. The method should be used as a standard machine learning technique.

2.5. Stacked Autoencoders (SAEs) with Random Forest (RF)

An autoencoder (AE) is a type of neural network that consists of two main components: an encoder and a decoder, as shown in Figure 4a. The model learns the most important features of the input data and reconstructs the original input data through encoding and decoding processes [17]. Typically, the encoding phase maps the input data to a hidden layer using a nonlinear activation function, while the decoding phase maps the hidden layer back to the output layer. In essence, an autoencoder can be viewed as a compact deep learning model composed of an input layer, a hidden layer, and an output layer.

A Stacked Autoencoder (SAE) consists of multiple autoencoders stacked on top of each other (Figure 4b), where each autoencoder is trained individually in an unsupervised manner using a greedy, layer-by-layer training approach. This method helps address the gradient issues commonly encountered during traditional multi-layer neural network training [18]. The output from one hidden layer serves as the input to the next hidden layer. Once the model is pre-trained, fine-tuning is performed to adjust the parameters and achieve optimal performance. The output of the final hidden layer is then used as the deep feature representation of the input data.

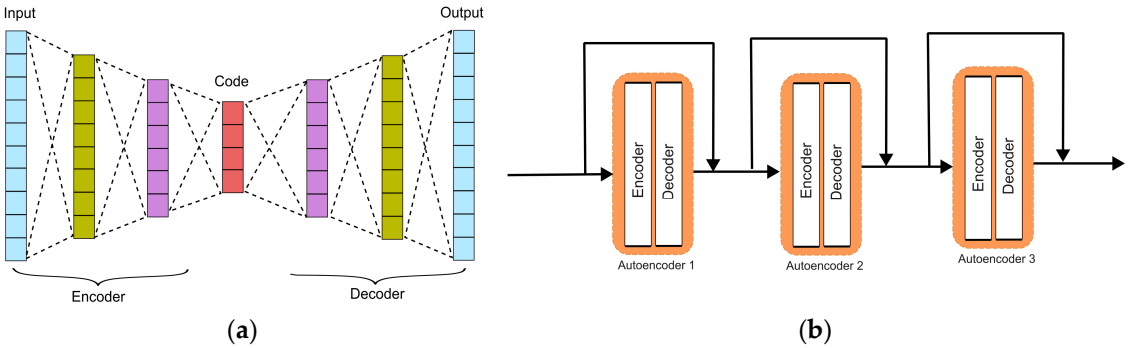


Figure 4. Structure of an (**a**) autoencoder and a (**b**) Stacked Autoencoder.

In this study, a Stacked Autoencoder in combination with Random Forest was implemented for regression. For training the SAE network, the "Adam" optimizer and Root Mean Square Error (RMSE) loss function with a learning rate of 0.001 and batch size of 8 are used. Once the training was completed, each pixel in the HSI dataset was encoded by using only the encoder part of the SAE architecture to obtain the reduced dataset, and the output was fed to the Random Forest regressor. The architecture of the Stacked Autoencoder with Random Forest regression used in this research is shown in Figure 5.

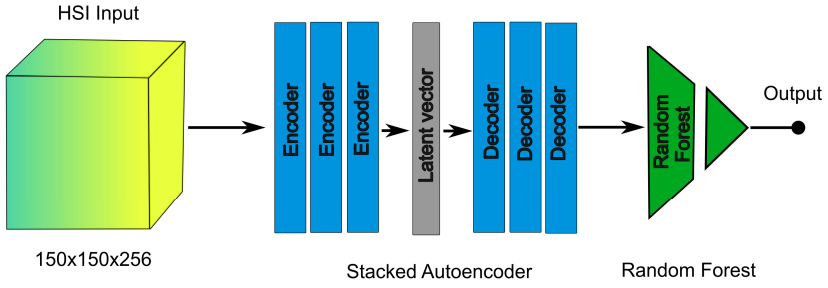


Figure 5. Stacked Autoencoder in a combination with Random Forest.

2.6. Convolutional Neural Networks

In recent years, CNNs have been widely applied in food category recognition [19]. In this study, three types of CNN architectures—1D, 2D, and 3D—were utilized to extract hyperspectral image features for estimating β-carotene concentrations. CNNs are deep neural networks designed to process multidimensional image data through forward and backward propagation, leveraging convolutional layers, pooling layers, and activation functions [20,21]. Convolutional layers serve as feature extractors by performing dot-product operations between the input vector and trainable weights and biases, followed by an activation function to introduce nonlinearity. Pooling layers further refine these features by reducing spatial dimensions and retaining essential patterns. The learning process optimizes the model by minimizing a loss function, with backpropagation computing the loss gradients across network layers. In this study, CNN networks were implemented using the TensorFlow framework. The following sections explore the three primary CNN architectures applied in hyperspectral analysis:

- 1D-CNN (One-Dimensional Convolutional Neural Network): 1D-CNNs process one-dimensional sequential data, making them suitable for both time-series and spectral data processing analyses. In hyperspectral analysis, 1D-CNNs use spectral information at the pixel level, ignoring spatial dependencies [22]. They are computationally efficient, making them ideal for real-time applications [23].
- 2D-CNN (Two-Dimensional Convolutional Neural Network): It operates on two-dimensional image data, using convolutional filters to capture spatial features. They

are commonly applied in RGB and hyperspectral images, often with prior spectral dimension reduction [24]. In hyperspectral imaging, 2D-CNNs analyzes local texture and spatial relationships within a given spectral band [25].

- 3D-CNN (Three-Dimensional Convolutional Neural Network): These types of networks simultaneously process both spectral and spatial information using three-dimensional convolutional filters [20]. This approach retains relationships across spectral bands and spatial features, making 3D-CNNs highly effective for hyperspectral image analysis. However, they require significant computational resources. Depending on the research requirements, different architectures are applied to achieve different results.

2.6.1. Development of 1D-CNN Architecture

The 1D convolutional neural network (1D-CNN) was designed to process the hyperspectral data by focusing on spectral features along each pixel's spectral profile, leveraging the dimensionality of the spectral bands. For this task, the spectral features were extracted by averaging across spatial dimensions, resulting in a 1D input vector for each pixel. The 1D-CNN architecture consisted of several convolutional layers followed by pooling and fully connected layers to enable feature learning and regression prediction. Figure 6 is a representation of the layer structure with the corresponding filter size.

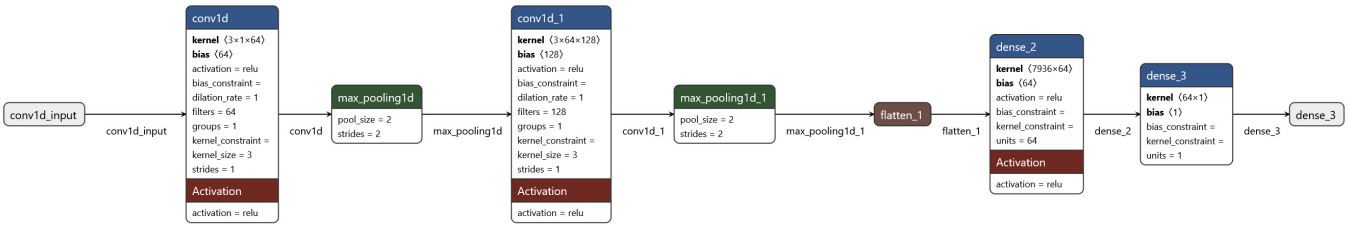


Figure 6. Structure of 1D-CNN network architecture.

2.6.2. Development of 2D-CNN Architecture

The 2D convolutional neural network (2D-CNN) was developed to model the spatial variability in the hyperspectral images while reducing spectral dimensionality through prior averaging across bands. Specifically, each image sample was preprocessed by averaging, resulting in a 2D input matrix per sample. The resulting spatial maps (e.g., of size 150 × 150) were used as input to the network. The architecture of the network is shown in Figure 7.

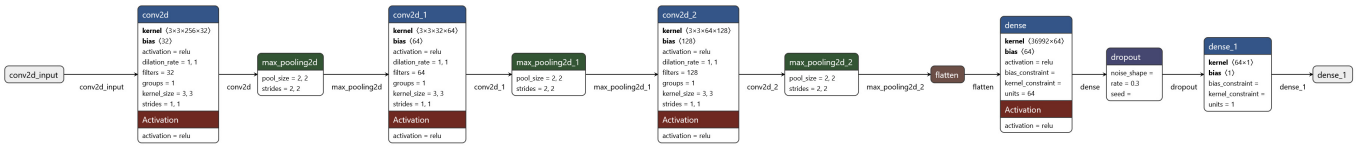


Figure 7. Structure of 2D-CNN network architecture.

2.6.3. Development of 3D-CNN Architecture

The 3D convolutional neural network (3D-CNN) was designed to capture both spectral and spatial information from hyperspectral image cubes of apricot samples, with dimensions of 150 × 150 pixels and 256 spectral bands. The network architecture consisted of three convolutional blocks, each incorporating 3 × 3 × 3 convolutional layers with ReLU activation (CReLU), batch normalization, and 2 × 2 × 2 max-pooling to progressively reduce the spatial and spectral dimensions while retaining the most relevant features. The response variable was the concentration of a specific quality parameter (e.g., β-carotene),

obtained through laboratory analysis and used as ground truth for regression. The model was implemented in TensorFlow and trained using the Adam optimizer with a learning rate of 0.001 and Root Mean Squared Error (RMSE) as the loss function. The structure of the network is shown in Figure 8.

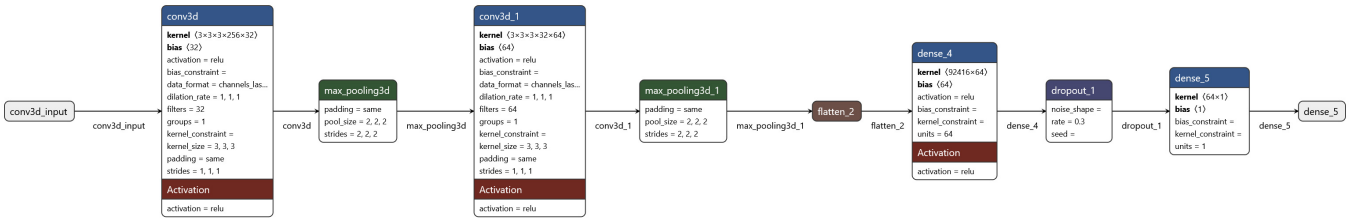


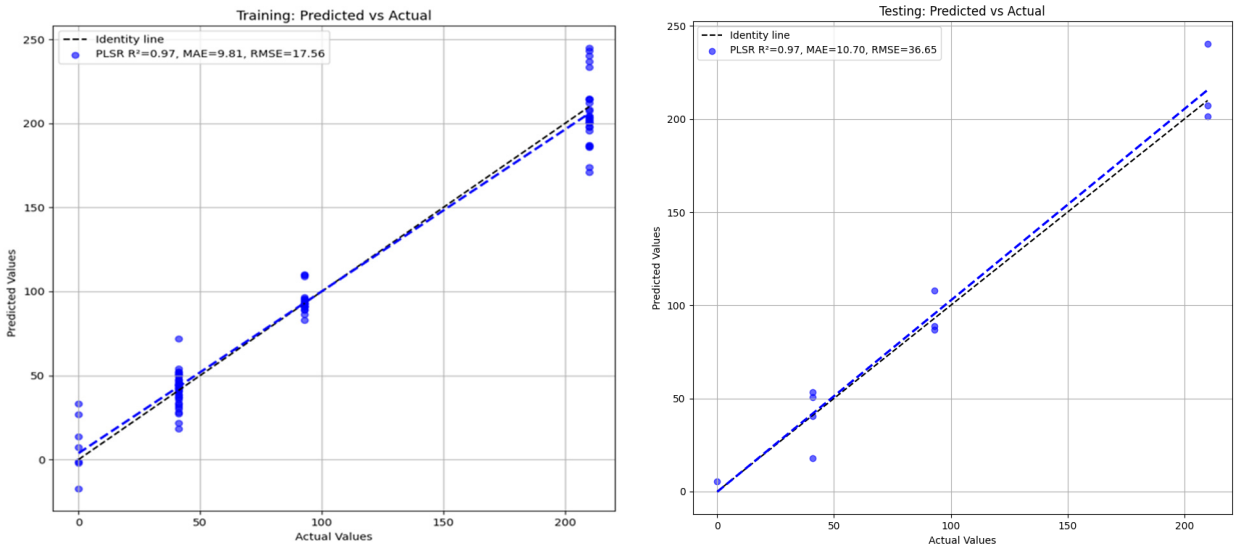
Figure 8. Structure of 3D-CNN network architecture.

3. Results and Discussion

In this study, a classical Partial Least Squares Regression (PLSR) model, an approach combining Stacked Autoencoders (SAEs) with Random Forest (RF), as well as various types of Convolutional Neural Networks (CNNs) for modeling β-carotene content were investigated. Hyperspectral images, captured in the near-infrared (NIR) region, were collected during the drying process to analyze and predict the β-carotene levels. The performance of the different predictive models was assessed based on their ability to predict the β-carotene content from hyperspectral images. Several evaluation metrics, such as R^2 (coefficient of determination), Mean Absolute Error (MAE), and Root Mean Squared Error (RMSE), were used to quantify the accuracy of the models. Based on the nature of the models used, two evaluation strategies were adopted. The 2D-CNN and 3D-CNN architectures operated on entire hyperspectral image cubes and therefore produced a single prediction per image, corresponding to the average β-carotene content. In contrast, models such as 1D-CNN, PLSR, and SAE-RF utilized individual spectral vectors extracted from the images and therefore could generate predictions for each individual pixel or region within the hyperspectral image. This enabled spatially resolved estimates of β-carotene content, allowing for more detailed analysis and visualization of distribution patterns across the sample.

3.1. PLS Model Results

The PLSR model was applied to predict the β-carotene content based on spectral data extracted from the hyperspectral images and transformed using the mean spectrum. The model's performance was evaluated by comparing the predicted values to the actual β-carotene measurements. The training and testing processes are shown in Figure 9. The R^2 value for the PLSR model was found to be 0.97 for both training and testing, indicating excellent predictive performance and minimal overfitting. The values of MAE_t = 9.81 and $RMSE_t$ = 17.56 for training, and MAE_p = 10.7 and $RMSE_p$ = 36.65 for testing, indicate a reasonable predictive accuracy, with low average and root-mean-squared errors across both training and testing datasets. In the figures, two lines are shown: the identity line and the trend line. Since these lines are closely aligned, it suggests that the model exhibits good predictive performance.

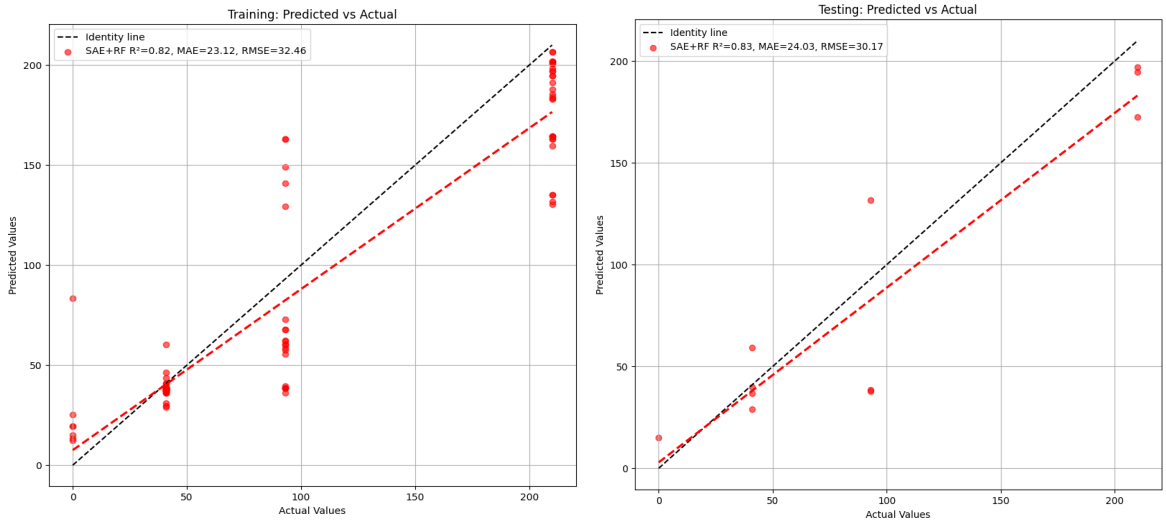


(**a**) (**b**)

Figure 9. Predictive models for PLSR: (**a**) training; (**b**) testing.

3.2. SAE-RF Model Results

The combination of Stacked Autoencoders (SAEs) and Random Forest (RF) was used to improve prediction accuracy by learning complex patterns in the data. The model was trained on mean-spectrum hyperspectral data. The results from training and testing are presented in Figure 10. The SAE-RF model achieved satisfactory performance, with Rt2 = 0.82 and Rp2 = 0.83, indicating minimal overfitting or underfitting. The MAE and RMSE values were MAEt = 23.12, MAEp = 24.03, RMSEt = 32.46, and RMSEp = 30.17, respectively. The similarity of these values suggests that the model performs consistently across both the training and testing datasets.



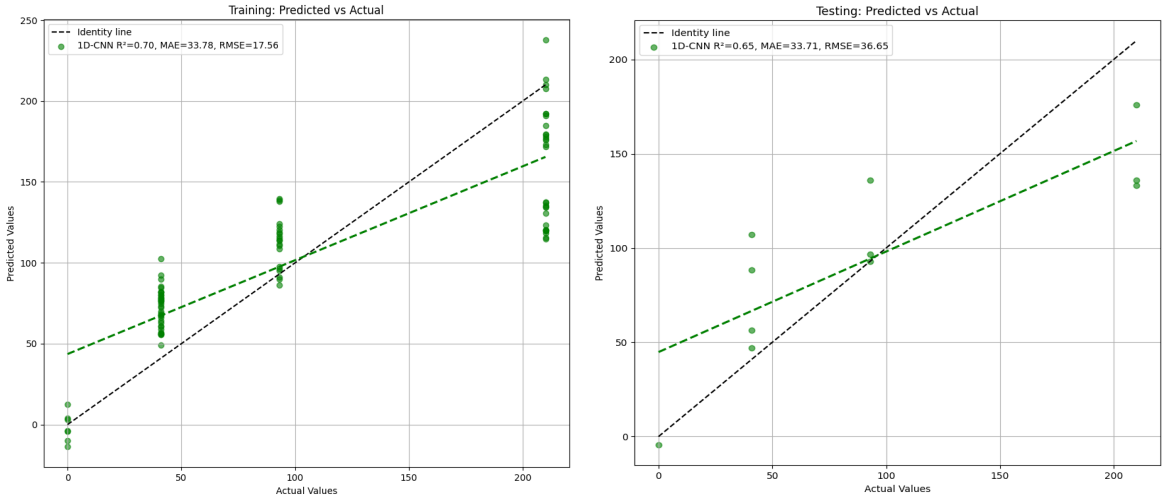
(**a**) (**b**)

Figure 10. Predictive models for SAE-RF: (**a**) training; (**b**) Testing.

3.3. CNN Models Results

Several Convolutional Neural Network (CNN) models were trained to predict β-carotene content from the hyperspectral images. Three different types of CNN architectures were employed: 1D-CNN, 2D-CNN, and 3D-CNN. The results for each model were as follows:

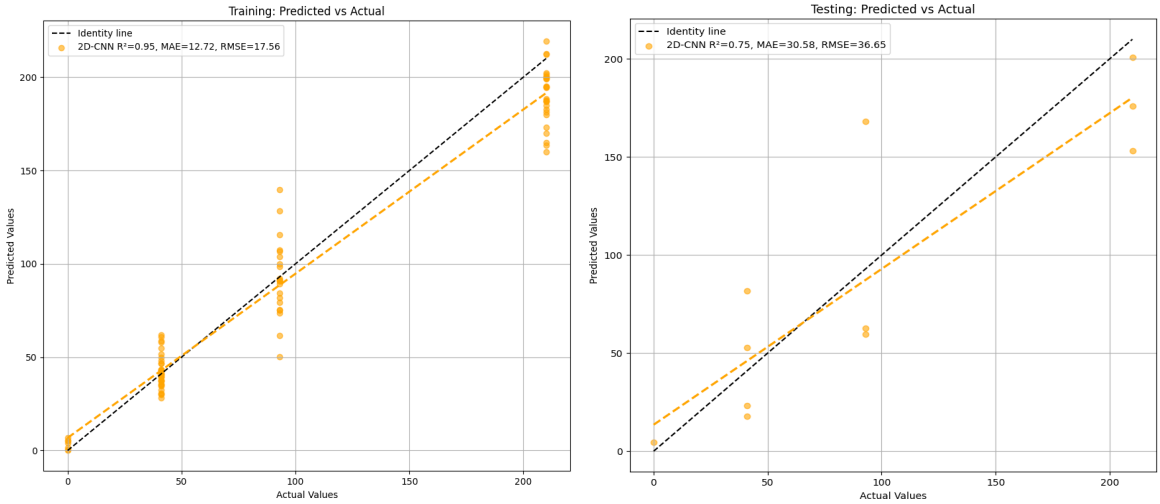
- 1D-CNN: The training and testing processes are given in Figure 11. The 1D-CNN model showed an R^2 value of 0.7 for training and 0.65 for testing, The 1D-CNN model showed an R^2 value of 0.7 for training and 0.65 for testing, indicating moderate but acceptable predictive performance with reasonable generalization ability, though there is room for improvement in capturing the underlying patterns in the data. The values for MAEt = 33.7 and RMSEt = 17.56 for training and MAEp = 33.71 and RMSEp = 36.65 for predicting.



(**a**) (**b**)

Figure 11. Predictive models for 1D-CNN: (**a**) training; (**b**) Testing.

- 2D-CNN: The training and testing processes are presented in Figure 12. The 2D-CNN model demonstrated strong performance, achieving an R^2 value of 0.95, an MAE of 12.72, and an RMSE of 17.56 on the training set. On the test set, the model achieved an R^2 value of 0.75, an MAE of 30.58, and an RMSE of 36.65. These results indicate excellent fit on the training data, but also suggest some degree of overfitting. Nevertheless, the model still explains 75% of the variance in the unseen data, which may be sufficient for the intended application.



(**a**) (**b**)

Figure 12. Predictive models for 2D-CNN: (**a**) training; (**b**) Testing.

- 3D-CNN: The training and testing processes are presented in Figure 13. The 3D-CNN model achieved an R^2 value of 0.84 for training and 0.69 for testing, with

MAE and RMSE values of 12.72 and 17.56 for training, and 30.58 and 36.65 for testing, respectively. The model demonstrates good performance on the training set, indicating its ability to capture underlying patterns in the data. However, the drop in performance on the testing set suggests potential overfitting. This discrepancy between training and testing results implies that the model may have learned specific features of the training data that do not generalize well to unseen samples. Such overfitting could be attributed to the limited size of the dataset or the high complexity of the 3D-CNN model relative to the amount of training data.

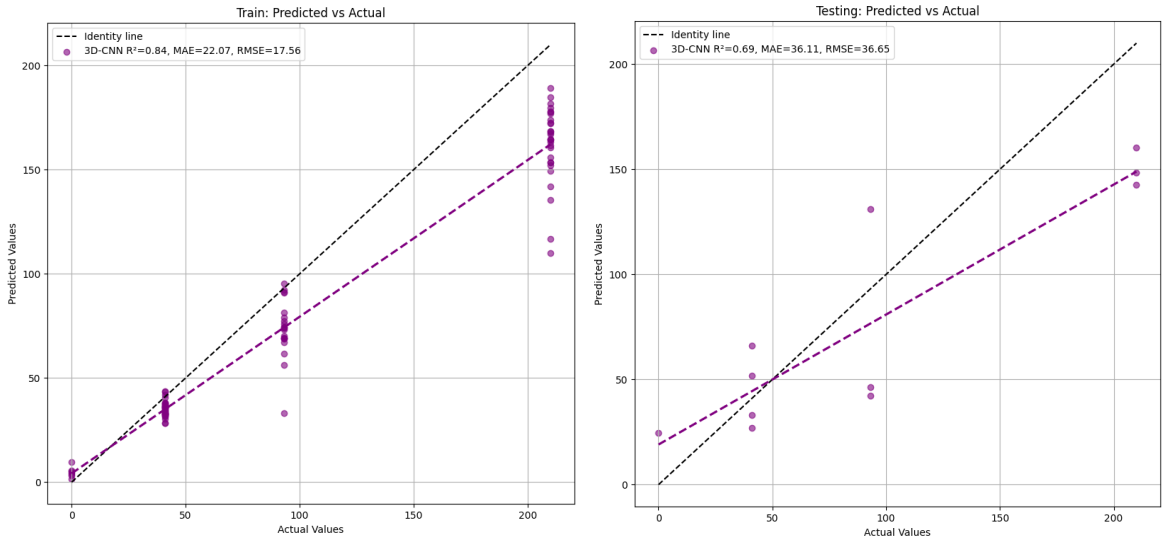


Figure 13. Predictive models for 3D-CNN: (**a**) training; (**b**) Testing.

3.4. Comparison of Regression Models

The training and testing of all models were assessed using R^2 (coefficient of determination), RMSE (Root Mean Squared Error), and MAE (Mean Absolute Error). Each model was trained to predict the β-carotene concentration as a quality parameter of apricots. The regression performance for each model is summarized in Table 1.

Table 1. Structure of 3D-CNN Network.

	Train			Test		
Model	**R^2**	**RMSE**	**MAE**	**R^2**	**RMSE**	**MAE**
PLSR	0.97	36.65	10.7	0.97	17.56	9.81
SAE-RF	0.82	32.46	23.12	0.83	30.17	24.03
1D-CNN	0.7	17.57	33.78	0.75	36.65	30.58
2D-CNN	0.95	17.56	12.72	0.75	36.65	30.58
3D-CNN	0.84	17.56	22.07	0.69	36.65	36.11

4. Conclusions

In this study, various models for predicting β-carotene content using hyperspectral images captured in the near-infrared (NIR) region during the drying process were evaluated. The investigated models include a classical Partial Least Squares Regression (PLSR), a combination of Stacked Autoencoders (SAEs) and Random Forest (RF), as well as several types of Convolutional Neural Networks (CNNs), including 1D-CNN, 2D-CNN, and 3D-CNN. The PLSR model demonstrated excellent predictive performance, achieving an R^2 value of 0.97 for both training and testing, indicating minimal overfitting and

high generalization capability. The SAE-RF model also showed strong and consistent results, with R^2 values of 0.82 for training and 0.83 for testing, confirming its robustness and reliability across datasets. While not outperforming the PLSR model, SAE-RF still provided accurate and stable predictions. The CNN models displayed more variability in performance. The 1D-CNN yielded moderate but acceptable results, suggesting it can capture essential spectral patterns. The 2D-CNN model showed strong performance during training (R^2 = 0.95), but a drop in test performance (R^2 = 0.75) pointed to overfitting. Similarly, the 3D-CNN model performed well on training data but experienced a decline in test accuracy, again indicating potential overfitting. Overall, while CNN models—especially 2D-CNN—show potential for modeling complex spatial-spectral relationships in hyperspectral data, their tendency to overfit highlights the need for further refinement. In contrast, the PLSR and SAE-RF models provided more consistent and generalizable results, with PLSR emerging as the most robust approach. Future work should focus on improving the CNN models by applying advanced regularization techniques, increasing the dataset size, and optimizing architectural designs to better generalize across unseen data.

Funding: This research received no external funding.

Institutional Review Board Statement: Not applicable.

Informed Consent Statement: Not applicable.

Data Availability Statement: Data are available from the corresponding author upon reasonable request.

Conflicts of Interest: The author declares no conflicts of interest.

Abbreviations

The following abbreviations are used in this manuscript:

SAE	Stacked Autoencoder
DM	Dry Matter
BPNN	Backpropagation Neural Network
CNN	Convolutional Neural Network
SAE-RF	Stacked Autoencoder in Combination with Random Forest
PLSR	Partial Least Square Regression
MAE	Mean Absolute Error
RMSE	Root Mean Square Error
PCA	Principal Component Analysis
AE	Autoencoder

References

1. Elisabeth, J.M.B.; Esther, N.D.K.; Susan, G.B.d.K.; Joyce, S.; Arend, G.J.A.; Niels, F.M.K.; Theo, J.M.R. Hyperspectral imaging for tissue classification, a way toward smart laparoscopic colorectal surgery. *J. Biomed. Opt.* **2019**, *24*, 016002. [CrossRef]
2. Wang, B.; Sun, J.; Xia, L.; Liu, J.; Wang, Z.; Li, P.; Sun, X. The Applications of Hyperspectral Imaging Technology for Agricultural Products Quality Analysis: A Review. *Food Rev. Int.* **2023**, *39*, 1043–1062. [CrossRef]
3. Parrag, V.; Gillay, Z.; Kovács, Z.; Zitek, A.; Böhm, K.; Hinterstoisser, B.; Baranyai, L. Application of hyperspectral imaging to detect toxigenic Fusarium infection on cornmeal. *Prog. Agric. Eng. Sci.* **2020**, *16*, 51–60. [CrossRef]
4. Wang, L.; Jin, J.; Song, Z.; Wang, J.; Zhang, L.; Rehman, T.U.; Tuinstra, M.R. LeafSpec: An accurate and portable hyperspectral corn leaf imager. *Comput. Electron. Agric.* **2020**, *169*, 105209. [CrossRef]
5. Chen, J.; Chen, S.; Zhou, P.; Qian, Y. Deep neural network based hyperspectral pixel classification with factorized spectral-spatial feature representation. *IEEE Access* **2019**, *7*, 81407–81418. [CrossRef]
6. Jung, D.H.; Kim, J.D.; Kim, H.Y.; Lee, T.S.; Kim, H.S.; Park, S.H. A hyperspectral data 3D convolutional neural network classification model for diagnosis of gray mold disease in strawberry leaves. *Front. Plant Sci.* **2022**, *13*, 837020. [CrossRef] [PubMed]

7. Liu, K.H.; Yang, M.H.; Huang, S.T.; Lin, C. Plant species classification based on hyperspectral imaging via a lightweight convolutional neural network model. *Front. Plant Sci.* **2022**, *13*, 855660. [CrossRef]
8. Nie, P.; Zhang, J.; Feng, X.; Yu, C.; He, Y. Classification of hybrid seeds using near-infrared hyperspectral imaging technology combined with deep learning. *Sens. Actuators B Chem.* **2019**, *296*, 126630. [CrossRef]
9. Yu, Z.; Fang, H.; Zhangjin, Q.; Mi, C.; Feng, X.; He, Y. Hyperspectral imaging technology combined with deep learning for hybrid okra seed identification. *Biosyst. Eng.* **2021**, *212*, 46–61. [CrossRef]
10. Simonyan, K.; Vedaldi, A.; Zisserman, A. Deep inside convolutional networks: Visualising image classification models and saliency maps. *arXiv* **2013**, arXiv:1312.6034. [CrossRef]
11. Su, Z.; Zhang, C.; Yan, T.; Zhu, J.; Zeng, Y.; Lu, X.; Fan, L. Application of hyperspectral imaging for maturity and soluble solids content determination of strawberry with deep learning approaches. *Front. Plant Sci.* **2021**, *12*, 736334. [CrossRef]
12. Zhu, H.; Chu, B.; Zhang, C.; Liu, F.; Jiang, L.; He, Y. Hyperspectral Imaging for Presymptomatic Detection of Tobacco Disease with Successive Projections Algorithm and Machine-learning Classifiers. *Sci. Rep.* **2017**, *7*, 4125. [CrossRef]
13. Dejanov, M. Evaluation of β-Carotene Content in Apricots during the Drying Process Using Visual and Near-Infrared Spectroscopy. In Proceedings of the 8th International Conference on Energy Efficiency and Agricultural Engineering (EE&AE), Ruse, Bulgaria, 30 June 2022. [CrossRef]
14. Wold, S.; Sjöström, M.; Eriksson, L. PLS-regression: A basic tool of chemometrics. *Chemom. Intell. Lab. Syst.* **2001**, *58*, 109–130. [CrossRef]
15. Gowen, A.A.; O'Donnell, C.P.; Cullen, P.J.; Downey, G.; Frias, J.M. Hyperspectral imaging—An emerging process analytical tool for food quality and safety control. *Trends Food Sci. Technol.* **2007**, *18*, 590–598. [CrossRef]
16. Huang, H.; Yu, H.; Xu, H.; Ying, Y. Near infrared spectroscopy for on/in-line monitoring of quality in foods and beverages: A review. *J. Food Eng.* **2008**, *87*, 303–313. [CrossRef]
17. Mienye, I.D.; Swart, T.G. Deep Autoencoder Neural Networks: A Comprehensive Review and New Perspectives. *Arch. Comput. Methods Eng.* **2025**, *32*, 1–28. [CrossRef]
18. Geoffrey, E.H.; Simon, O.; Yee-Whye, T. A Fast-Learning Algorithm for Deep Belief Nets. *Neural Comput.* **2006**, *18*, 1527–1554. [CrossRef]
19. Kawano, Y.; Yanai, K. Food Image Recognition with Deep Convolutional Features. In Proceedings of the 2014 ACM International Joint Conference on Pervasive and Ubiquitous Computing: Adjunct Publication, Seattle, WA, USA, 13–17 September 2014; pp. 589–593. [CrossRef]
20. Li, Y.; Zhang, H.; Shen, Q. Spectral–spatial classification of hyperspectral imagery with 3D convolutional neural network. *Remote Sens.* **2017**, *9*, 67. [CrossRef]
21. Zhang, L.; Wang, Y.; Li, H. A Review of Convolutional Neural Networks in Computer Vision. *Artif. Intell. Rev.* **2024**, *57*, 99. [CrossRef]
22. Chen, Y.; Jiang, H.; Li, C.; Jia, X.; Ghamisi, P. Deep Feature Extraction and Classification of Hyperspectral Images Based on Convolutional Neural Networks. *IEEE Trans. Geosci. Remote Sens.* **2016**, *54*, 6232–6251. [CrossRef]
23. Zhao, W.; Du, S. Spectral–Spatial Feature Extraction for Hyperspectral Image Classification: A Dimension Reduction and Deep Learning Approach. *IEEE Trans. Geosci. Remote Sens.* **2016**, *54*, 4544–4554. [CrossRef]
24. Makantasis, K.; Karantzalos, K.; Doulamis, A.; Doulamis, N. Deep Supervised Learning for Hyperspectral Data Classification through Convolutional Neural Networks. In Proceedings of the IEEE International Geoscience and Remote Sensing Symposium (IGARSS), Milan, Italy, 26–31 July 2015; pp. 4959–4962. [CrossRef]
25. Roy, S.K.; Krishna, G.; Dubey, S.R.; Chaudhuri, B.B. HybridSN: Exploring 3-D–2-D CNN Feature Hierarchy for Hyperspectral Image Classification. *IEEE Geosci. Remote Sens. Lett.* **2020**, *17*, 277–281. [CrossRef]

Disclaimer/Publisher's Note: The statements, opinions and data contained in all publications are solely those of the individual author(s) and contributor(s) and not of MDPI and/or the editor(s). MDPI and/or the editor(s) disclaim responsibility for any injury to people or property resulting from any ideas, methods, instructions or products referred to in the content.